

# Quantum thermodynamics, quantum correlations and quantum coherence in accelerating Unruh-DeWitt detectors in both steady and dynamical state

Omar Bachain,<sup>1</sup> Mohamed Amazioug,<sup>2,\*</sup> and Rachid Ahl Laamara<sup>1,3</sup>

<sup>1</sup>*LPHE-Modeling and Simulation, Faculty of Sciences, Mohammed V University in Rabat, Rabat, Morocco*

<sup>2</sup>*LPTHE-Department of Physics, Faculty of Sciences, Ibnou Zohr University, Agadir 80000, Morocco*

<sup>3</sup>*Centre of Physics and Mathematics, CPM, Faculty of Sciences, Mohammed V University in Rabat, Rabat, Morocco*

(Dated: December 23, 2025)

We investigate the interplay between quantum thermodynamics, quantum correlations, and quantum coherence within the framework of the Unruh-DeWitt (UdW) detector model. By analyzing both the steady and dynamical states of various quantum resources (including steerability, entanglement, quantum discord, and coherence), we study how these resources evolve under Markovian and non-Markovian environments. Furthermore, we investigate the impact of both the Unruh temperature and the energy levels on three key quantum phenomena: thermodynamic evolution, quantum correlations, and quantum coherence, considering different initial state preparations. The hierarchical structure relating quantum correlations and quantum coherence is determined. We further examine the thermodynamic performance of a quantum heat engine, highlighting the influence of memory effects and classical correlations on heat exchange, work extraction, and efficiency. Our results reveal that non-Markovian dynamics can enhance the preservation of quantum correlations and improve the engine's efficiency compared to purely Markovian regime. These findings provide insights into the role of quantum correlations and quantum coherence in quantum thermodynamic processes and open avenues for optimizing quantum devices operating in relativistic or open-system settings.

**Keywords:** Quantum correlations, Unruh-DeWitt detector, Quantum thermodynamics, Quantum heat engines, Markovian, Non-Markovian, Entanglement, Quantum coherence.

## I. INTRODUCTION

In 1935, Einstein, Podolsky, and Rosen (EPR) introduced a thought experiment, known as the EPR paradox, which posed fundamental challenges to the foundations of quantum mechanics. This paradox revealed the existence of nonlocal correlations between quantum systems, indicating that a measurement performed on one system can instantaneously affect the state of another, spatially separated system [1, 2]. Bell's theorem later demonstrated that local hidden variable theories are incapable of accounting for all nonlocal correlations arising from local quantum measurements on spatially separated systems [3].

Within this framework, quantum steering has emerged as a particularly intriguing phenomenon in quantum mechanics [4, 5], highlighting intricate correlations between entangled particles [6]. Quantum steering occurs when the measurement of one particle (commonly referred to as Alice) influences the state of another particle (Bob), irrespective of the spatial separation between them, reflecting the inherent nonlocality of quantum mechanics. Leveraging their shared entanglement, Alice can effectively "steer" Bob's state [7].

Beyond entanglement, recent studies have demonstrated that quantum correlations can persist even in separable states [8–10]. In this context, geometric quantum discord (GQD) provides an extended framework for characterizing nonclassical correlations beyond entanglement [11], offering a powerful tool for quantifying quantum resources. Geometric approaches, such as the Schatten 1-norm quantum discord, have proven particularly useful in a variety of systems, including metal complexes [12]. These developments refine our understanding of

quantum resource quantification and further expand the potential applications of quantum information protocols [13, 14].

Quantum coherence, a central concept in quantum physics, refers to the capacity of a system to exist in superposition states in which multiple configurations coexist simultaneously. This property underlies a wide range of quintessentially quantum phenomena, including interference and quantum optical effects [15, 16]. However, coherence is highly sensitive to environmental disturbances and is progressively suppressed through decoherence [17], a mechanism by which quantum systems lose their non-classical features due to interactions with their surroundings. The interplay between coherence and decoherence plays a crucial role in several domains, notably quantum thermodynamics [18, 19], where it influences the performance and efficiency of quantum heat engines, and the physics of quantum dots [20, 21], which constitute key building blocks for quantum information technologies.

A quantum heat engine (QHE) represents a fundamental platform for investigating problems in quantum thermodynamics (QT), a rapidly developing field that examines thermodynamic processes within the framework of quantum dynamics [22–25]. Building upon classical thermodynamic cycles, researchers have proposed their quantum counterparts, enabling the systematic study of QHEs and their efficiencies [26–35]. The physical characteristics of QHEs, as well as quantum refrigerators, have been extensively explored in the literature. Typically, a QHE consists of a working substance coupled to two distinct thermal reservoirs—a hot bath and a cold bath. To rigorously analyze the operation of QHEs, both isothermal and isochoric processes are employed. Various quantum systems have been considered as working substances, including single spins [36], harmonic oscillators [37–42], ideal quantum gases [43, 44], Heisenberg spin models [45, 46], and two- or three-level systems [47–49]. More recently, alternative working materials such as quantum

\* [m.amazioug@uiz.ac.ma](mailto:m.amazioug@uiz.ac.ma)

dots [50, 51] and Heisenberg XX, XXZ, or XYZ spin models with Dzyaloshinskii-Moriya interactions (DMI) [52–54] have also been investigated, highlighting the growing diversity of quantum systems utilized in heat engine designs.

Quantum correlations, such as entanglement and quantum discord, play a central role in quantum thermodynamics, where they serve as essential resources for optimizing work extraction, energy transfer, and the performance of microscopic thermal machines. In relativistic settings [55–57], the study of these correlations becomes particularly significant, as non-inertial motion can strongly influence the thermodynamic behavior of quantum systems. The UdW detector model [58], which describes the interaction between point-like detectors and a quantum field, provides a powerful theoretical framework for investigating these phenomena. When a detector undergoes uniform acceleration, the Unruh effect causes it to perceive the quantum vacuum as a thermal bath, thereby introducing an intrinsic source of noise and decoherence. This perceived thermalization directly affects the quantum correlations shared between detectors and, consequently, modifies thermodynamic processes such as entropy production, heat flow, and work extraction. Thus, the use of the UdW model allows for a detailed exploration of how relativistic effects degrade, reshape, or even generate quantum correlations, offering new insights into quantum thermodynamics in accelerating frames and guiding the development of robust quantum technologies capable of operating in non-inertial environments.

The primary objective of this work is to explore the hierarchy of quantum correlations—including quantum steering, entanglement, geometric quantum discord (GQD), and quantum coherence—within the framework of quantum thermodynamics for a two-UdW-detector system. We begin by analyzing the system in the absence and in the presence of decoherence, a crucial step for improving the robustness of qubits against environmental noise. Subsequently, by investigating the interplay between classical and quantum correlations in both Markovian and non-Markovian environments, we aim to enhance the stability of the system under various noise regimes. Furthermore, this study assesses the influence of variations in the energy level spacing of the atom ( $\omega$ ) and the initial state selection parameter ( $\Delta_0$ ) on the thermodynamic behavior of UdW devices, particularly as a function of temperature. Finally, we investigate this quantum system as a working substance in both a quantum heat engine and a refrigerator within the framework of the Stirling cycle.

The structure of this article is organized as follows: Section II (Model) introduces the two-UdW-detector system and its thermal density operator, examining its dynamics under a correlated dephasing channel; Section III (Correlations) provides a comprehensive overview of fundamental quantum concepts (steering, entanglement, geometric quantum discord, and coherence) and presents the detailed analysis and results of our study; Section IV (Discussion) discusses the implications of these findings within the broader research context; Section V (Thermodynamics) addresses the Stirling cycle and evaluates its performance; and finally, Section VI (Conclusion) concludes the article and provides additional discussion.

## II. THEORY AND MODEL

### A. Hamiltonian and matrix density

To explore the behavior of two uniformly accelerated UdW detectors in a 3 + 1-dimensional Minkowski spacetime [58–60], we describe the detectors using the framework of open quantum systems. In this approach, the system undergoes a non-unitary evolution of its density matrix due to decoherence and dissipation effects arising from its interaction with the surrounding environment. Each detector is represented as a two-level quantum system, and the overall dynamics are governed by the following total Hamiltonian [61]

$$\mathcal{H} = \mathcal{H}_0 + \mathcal{H}_\phi + \mathcal{H}_I, \quad (1)$$

where,  $\mathcal{H}_0$  represents the Hamiltonian of two independent detectors in the standard co-moving frame. The internal dynamics of each two-level detector is governed by a matrix  $2 \times 2$ , and  $\mathcal{H}_0$  can be concisely expressed as

$$\mathcal{H}_0 = \frac{\omega}{2} \left( \sigma_3^{(A)} \otimes \mathbb{I}^{(B)} + \mathbb{I}^{(A)} \otimes \sigma_3^{(B)} \right), \quad (2)$$

where  $\omega$  denotes the energy level spacing of the atom and  $\sigma_i^{(m)}$  being the Pauli matrices, and  $m = A, B$  labels the different atoms.  $\mathcal{H}_\phi$  is the Hamiltonian of free massless scalar fields  $\phi(t, x)$  satisfying the Klein-Gordon equation  $(g^{\mu\nu} \nabla_\mu \nabla_\nu) \phi(t, x) = 0$ . The interaction Hamiltonian can be written in dipole form [62]

$$\mathcal{H}_I = \mu \left[ \left( \sigma_2^{(A)} \otimes \mathbb{I}^{(B)} \right) \phi(t, x_1) + \left( \mathbb{I}^{(A)} \otimes \sigma_2^{(B)} \right) \phi(t, x_2) \right], \quad (3)$$

with  $\mu$  is a small dimensionless coupling constant. We study the time evolution of the detectors reduced density matrix,  $\rho_{AB}(\tau) = \text{tr}_I(\rho_{tot})$ , with  $\tau$  being the detectors proper time. The total system is initially separable,  $\rho_{tot}(0) = \rho_{AB}(0) |0\rangle \langle 0|$ , where  $|0\rangle$  denotes the field vacuum. As a closed system, its total density matrix follows the von Neumann equation  $i\dot{\rho}_{AB} = [\mathcal{H}, \rho_{tot}(\tau)]$ . In the weak-coupling limit, the open system dynamics of the detectors, obey the Kossakowski–Lindblad master equation [63, 64]

$$\frac{\partial \rho_{AB}(\tau)}{\partial \tau} = -i [\mathcal{H}_{\text{eff}}, \rho_{AB}(\tau)] + \mathcal{L} [\rho_{AB}(\tau)], \quad (4)$$

with

$$\mathcal{H}_{\text{eff}} = \mathcal{H}_0 - \frac{i}{2} \sum_{m=1}^2 \sum_{n=1}^2 C_{ij} \sigma_i^{(n)} \sigma_j^{(n)}, \quad (5)$$

and

$$\mathcal{L}[\rho] = \sum_{i,j=1,2,3} \sum_{\alpha,\beta=A,B} \frac{C_{ij}}{2} \left[ 2\sigma_j^{(\beta)} \rho \sigma_i^{(\alpha)} - \{\sigma_i^{(\alpha)}, \sigma_j^{(\beta)}\} \rho \right], \quad (6)$$

to define the Kossakowski matrix  $C_{ij}$ , we first introduce the Wightman function of the scalar field, which is given by

$$Y^+(x, x') = \langle 0 | \phi(x) \phi(x') | 0 \rangle. \quad (7)$$

The Fourier transform of the Wightman function is expressed as

$$Y(\lambda) = \int_{-\infty}^{+\infty} d\tau e^{i\lambda\tau} Y^+(\tau) = \int_{-\infty}^{+\infty} d\tau e^{i\lambda\tau} \langle \phi(\tau) \rangle \phi(0). \quad (8)$$

This Fourier transform allows for the determination of the coefficients  $C_{ij}$  through the following decomposition

$$C_{ij} = \frac{\gamma_+}{2} \delta_{ij} - i \frac{\gamma_-}{2} \epsilon_{ijk} \delta_{3,k} + \gamma_0 \delta_{3,i} \delta_{3,j}, \quad (9)$$

where

$$\gamma_{\pm} = Y(\omega) \pm Y(-\omega), \quad \gamma_0 = Y(0) - \frac{\gamma_+}{2}. \quad (10)$$

Moreover, the interaction with the external scalar field induces a Lamb shift contribution to the effective Hamiltonian

$$H_{\text{eff}} = \frac{1}{2} \tilde{\omega} \sigma_3, \quad (11)$$

where  $\tilde{\omega} = \omega + i[K(-\omega) - K(\omega)]$ , and  $K(\lambda)$  is the Hilbert transform of the Wightman function

$$K(\lambda) = \frac{1}{i\pi} \mathcal{P} \int_{-\infty}^{\infty} \frac{Y(\omega)}{\omega - \lambda} d\omega. \quad (12)$$

Along the trajectory of the accelerating detectors, the field's Wightman function satisfies the Kubo-Martin-Schwinger (KMS) condition

$$Y^+(\tau) = Y^+(\tau + i\beta), \quad (13)$$

where  $\beta = \frac{1}{T}$ . Equation (10) can be rewritten as

$$\gamma_+ = (1 + e^{-\beta\omega}) Y(\omega) \text{ and } \gamma_- = (1 - e^{-\beta\omega}) Y(\omega), \quad (14)$$

we define the ratio  $\gamma$  as

$$\gamma = \frac{\gamma_-}{\gamma_+} = \tanh\left(\frac{\beta\omega}{2}\right), \quad (15)$$

which depends exclusively on the Unruh temperature  $T$ , rather than on the local background correlator. In the Bloch representation of the UdW detector systems. Reconstructing the density matrix in the computational basis then gives the X-shaped stationary state [59]

$$\rho_{AB} = \begin{pmatrix} \rho_{11} & 0 & 0 & 0 \\ 0 & \rho_{22} & \rho_{23} & 0 \\ 0 & \rho_{32} & \rho_{33} & 0 \\ 0 & 0 & 0 & \rho_{44} \end{pmatrix}, \quad (16)$$

where

$$\rho_{11} = \frac{(3 + \Delta_0)(\gamma - 1)^2}{4(3 + \gamma^2)}, \quad \rho_{22} = \rho_{33} = \frac{(3 + \Delta_0)(\gamma + 1)^2}{4(3 + \gamma^2)} \quad (17)$$

$$\rho_{44} = \frac{3 - \Delta_0 - (\Delta_0 + 1)\gamma^2}{4(3 + \gamma^2)}, \quad \rho_{23} = \rho_{32} = \frac{\Delta_0 - \gamma^2}{2(3 + \gamma^2)}. \quad (18)$$

It is observed that the final equilibrium state of the two-detector system is determined by the ratio  $\gamma$ , which reflects the thermal effects associated with the Unruh phenomenon, as well as by the initial state parameters summarized by

$$\Delta_0 = \sum_i \text{Tr}[\rho_{AB}(0) \sigma_i^A \otimes \sigma_i^B].$$

Requiring  $\Delta_0$  to lie within the interval  $-3 \leq \Delta_0 \leq 1$  ensures the non-negativity of the initial state  $\rho_{AB}(0)$ .

## B. Preliminary Framework for Correlated Quantum Channels

This section formulates the evolution of a two-qubit thermal state under a correlated dephasing channel. The output state is obtained from the Kraus map [65-67]

$$\rho_{AB}(t) = \sum_{i,j=0}^3 L_{ij} \rho_{AB}(0) L_{ij}^\dagger, \quad L_{ij} = \sqrt{p_{ij}} (\sigma_i \otimes \sigma_j), \quad (19)$$

where the joint probability is given by [68]

$$p_{ij} = (1 - \mu) p_i p_j + \mu p_i \delta_{ij}, \quad (20)$$

introduce the correlation parameter  $\mu \in [0, 1]$ . For a pure dephasing process with  $p_0 = 1 - p$ ,  $p_3 = p$ , the temporal behavior of coherence is governed by a random telegraph signal through [67]

$$p(t) = \frac{1 - h(t)}{2}, \quad (21)$$

with

$$h(t) = \begin{cases} e^{-\frac{t}{2\tau}} \left[ \cos\left(\frac{\nu t}{2\tau}\right) + \frac{1}{\nu} \sin\left(\frac{\nu t}{2\tau}\right) \right], & 4\tau > 1 \\ e^{-\frac{t}{2\tau}} \left[ \cosh\left(\frac{\nu t}{2\tau}\right) + \frac{1}{\nu} \sinh\left(\frac{\nu t}{2\tau}\right) \right], & 4\tau < 1, \end{cases} \quad (22)$$

and  $\nu = \sqrt{|4\tau^2 - 1|}$ . The resulting attenuation of off-diagonal elements is described by

$$\zeta(t) = (1 - \mu) h^2(t) + \mu, \quad (23)$$

thus, the thermal density matrix evolves as

$$\rho_{AB}(t) = \begin{pmatrix} \rho_{11} & 0 & 0 & 0 \\ 0 & \rho_{22} & \zeta(t)\rho_{23} & 0 \\ 0 & \zeta(t)\rho_{32} & \rho_{33} & 0 \\ 0 & 0 & 0 & \rho_{44} \end{pmatrix}. \quad (24)$$

## III. QUANTUM RESOURCES MEASURES

### A. Quantum steering

Quantum steering represents a directional manifestation of quantum correlations, whereby local measurements on one qubit can non-locally influence the state of the other. Following the entropic formulation proposed by Schneeloch *et al.* [7], the steering criterion is expressed as

$$f_{AB} = H_x(B|A) + H_y(B|A) + H_z(B|A) \geq 2, \quad (25)$$

where  $H_i(B|A)$  denotes the conditional Shannon entropy corresponding to Pauli-basis measurements. A violation of this bound ( $f_{AB} < 2$ ) indicates the existence of steerability between the two subsystems.

The quantitative measure of steering is given by [69, 70]

$$S_{A \rightarrow B} = \max \left( 0, \frac{f_{AB} - 2}{f_{\max} - 2} \right), \quad f_{\max} = 6, \quad (26)$$

where

$$\begin{aligned} f_{AB} = & \frac{1}{2} \sum_{i=1}^4 \{ f_{x_i}^{AB} \log_2(f_{x_i}^{AB}) + f_{y_i}^{AB} \log_2(f_{y_i}^{AB}) + f_{z_i}^{AB} \log_2(f_{z_i}^{AB}) \} \\ & - \sum_{i=1}^2 \{ f_{x_i}^A \log_2(f_{x_i}^A) + f_{y_i}^A \log_2(f_{y_i}^A) + f_{z_i}^A \log_2(f_{z_i}^A) \}, \end{aligned} \quad (27)$$

and

$$\begin{aligned} f_{x_1}^{AB} = f_{x_2}^{AB} &= 1 + 2\rho_{23}, \quad f_{x_3}^{AB} = f_{x_4}^{AB} = 1 - 2\rho_{23}, \\ f_{y_1}^{AB} = f_{y_2}^{AB} &= 1 + 2\rho_{23}, \quad f_{y_3}^{AB} = f_{y_4}^{AB} = 1 - 2\rho_{23}, \\ f_{z_i}^{AB} &= 4\rho_{i,i}, \quad f_{x_1}^A = f_{x_2}^A = 1, \quad f_{y_1}^A = f_{y_2}^A = 1, \\ f_{z_1}^A = f_{z_2}^A &= 1 \pm (\rho_{11} - \rho_{44}), \end{aligned}$$

and the asymmetry between both directions is characterized by

$$\Delta_{12} = |S_{A \rightarrow B} - S_{B \rightarrow A}|. \quad (28)$$

For the considered UdW system, the structure of the Hamiltonian guarantees that  $S_{A \rightarrow B} = S_{B \rightarrow A}$ , indicating a bidirectional (two-way) steering. This formalism provides a rigorous framework for quantifying directional quantum correlations and for establishing the hierarchy among steering, entanglement, and other coherence-based measures in systems [7].

## B. Entanglement of formation

The entanglement of formation,  $\xi$ , for a bipartite pure state is defined as [71]

$$\xi(\rho_{AB}) = \mathcal{E}(C(\rho_{AB})), \quad (29)$$

with

$$\mathcal{E}(C(\rho_{AB})) = L \left[ \frac{1 + \sqrt{1 - C^2(\rho_{AB})}}{2} \right], \quad (30)$$

where  $L(x) = -x \log_2 x - (1 - x) \log_2(1 - x)$  and  $C$  denotes the concurrence. To measure the concurrence, we employ Wootters concurrence formalism [72–76]. For a general two-qubit density matrix  $\rho_{AB}$ , the concurrence is defined as

$$C(\rho_{AB}) = \max \left\{ 0, \sqrt{\nu_1} - \sqrt{\nu_2} - \sqrt{\nu_3} - \sqrt{\nu_4} \right\}, \quad (31)$$

where  $\nu_i$  ( $i = 1, \dots, 4$ ) are the eigenvalues, in decreasing order, of the non-Hermitian matrix

$$R = \rho_{AB} (\sigma_y \otimes \sigma_y) \rho_{AB}^* (\sigma_y \otimes \sigma_y), \quad (32)$$

with  $\rho_{AB}^*$  being the complex conjugate of  $\rho_{AB}$  in the computational basis and  $\sigma_y$  the Pauli matrix. For the considered  $X$ -type state, the concurrence can be expressed analytically as

$$C(\rho_{AB}) = 2 \max \{ 0, |\rho_{23}| - \sqrt{\rho_{11}\rho_{44}}, -\sqrt{\rho_{22}\rho_{33}} \}, \quad (33)$$

where  $\rho_{ij}$  denote the matrix elements of the density operator  $\rho_{AB}$ . The concurrence ranges from  $C = 0$  ( $\xi = 0$ ), corresponding to a separable state, to  $C = 1$  ( $\xi = 1$ ), representing a maximally entangled (Bell) state. This measure provides a reliable quantification of bipartite entanglement, particularly suitable for  $X$ -structured density matrices arising in UdW systems.

## C. Geometric quantum discord

The geometric approach constitutes a powerful framework for quantifying quantum correlations even beyond entanglement. In this context, the *geometric quantum discord* (GQD) is defined as the minimal Schatten 1-norm distance [77] between a bipartite quantum state  $\rho_{AB}$  and the closest classical–quantum state  $\rho_c$  [78, 79]

$$Q_G(\rho_{AB}) = \min_{\rho_c \in \Omega} \|\rho_{AB} - \rho_c\|_1, \quad (34)$$

where  $\|X\|_1 = \text{Tr}[\sqrt{X^\dagger X}]$  denotes the trace norm, and  $\Omega$  denotes the set of all classical–quantum states, each of which can be represented in the form

$$\rho_c = \sum_k p_k \Pi_{k,1} \otimes \rho_{k,2}, \quad (35)$$

where  $\{p_k\}$  is a probability distribution such that  $\sum_k p_k = 1$ ,  $\Pi_{k,1}$  are the orthogonal projectors associated with qubit 1, and  $\rho_{k,2}$  are the density operators of qubit 2. For a general two-qubit  $X$  state, the geometric quantum discord based on the Schatten 1-norm can be writes as [80, 81]

$$Q_G = \frac{1}{2} \sqrt{\frac{F_{11}^2 \max\{F_{22}^2 + F_{30}^2, F_{33}^2\} - F_{22}^2 \min\{F_{11}^2, F_{33}^2\}}{\max\{F_{22}^2 + F_{30}^2, F_{33}^2\} - \min\{F_{11}^2, F_{33}^2\} + F_{11}^2 - F_{22}^2}}. \quad (36)$$

The Fano-Bloch representation  $F$  of the two-qubit state provides the correlation matrix components  $F_{\mu\nu}$  as

$$F = \frac{1}{4} \sum_{\mu,\nu=0}^3 F_{\mu\nu} (\sigma_\mu \otimes \sigma_\nu), \quad (37)$$

where  $\sigma_\mu$  ( $\mu = 0, 1, 2, 3$ ) are the Pauli matrices, with  $\sigma_0$  being the identity operator. For the considered thermal  $X$ -state of the two qubits, the non-vanishing elements of  $F_{\mu\nu}$  are given by

$$\begin{aligned} F_{11} &= 2\rho_{23}, \quad F_{22} = 2\rho_{23}, \\ F_{33} &= 1 - 2(\rho_{22} + \rho_{33}), \quad F_{30} = 2(\rho_{11} + \rho_{22}) - 1. \end{aligned} \quad (38)$$

## D. Quantum Coherence

Quantum coherence represents a fundamental resource in quantum information theory, reflecting the superposition prin-

principle that underpins all quantum phenomena. Following Baumgratz *et al.* [82], it can be quantified by the  $l_1$ -norm of coherence, which measures the minimal distance between a given quantum state and the set of incoherent states. For a bipartite density matrix  $\rho_{AB}$  expressed in the computational basis as

$$\rho_{AB} = \sum_{i,j} \rho_{ij} |i\rangle\langle j|, \quad (39)$$

the  $l_1$ -norm of coherence is defined by the sum of the absolute values of the off-diagonal elements

$$C_{l_1}(\rho_{AB}) = \sum_{i \neq j} |\rho_{ij}|. \quad (40)$$

In the case of the UdW system considered here, the  $l_1$ -norm coherence can be explicitly evaluated from the density matrix elements as

$$C_{l_1}(\rho_{AB}) = 2|\rho_{23}|, \quad (41)$$

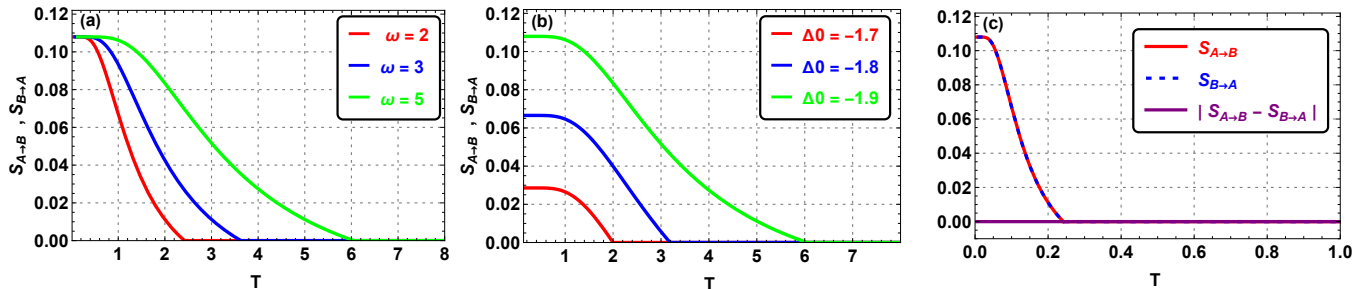


FIG. 1: (a) Quantum steerability  $S_{A \rightarrow B}$  and  $S_{B \rightarrow A}$  as a function of temperature  $T$  for different values of  $\omega$  with fixed  $\Delta_0 = -1.9$ ; (b) Quantum steerability versus  $T$  for different values of the initial state parameter  $\Delta_0$  with  $\omega = 5$ ; (c) Comparison of  $S_{A \rightarrow B}$ ,  $S_{B \rightarrow A}$ , and  $\Delta_{12}$  for  $\Delta_0 = -1.9$  and  $\omega = 0.2$ .

In Fig. 1(a), we present the quantum steerabilities  $S_{A \rightarrow B}$  and  $S_{B \rightarrow A}$  as functions of the temperature  $T$  for different values of  $\omega$ , while keeping the initial state parameter  $\Delta_0 = -1.9$ . Owing to the symmetry of the system, both steerabilities coincide, i.e.,  $S_{A \rightarrow B} = S_{B \rightarrow A}$ . For temperatures  $T \in [0, 0.4]$ , the steerability remains maximal for all values of  $\omega$ . Furthermore, the threshold temperature at which the steerability begins to decline shifts to higher values as  $\omega$  decreases. In the range  $T \in [0.4, 6]$ , the steerability exhibits a monotonic decrease, while its mag-

nitude becomes larger for smaller values of  $\omega$ , as illustrated in Fig. 1(a). Additionally, for  $T > 6$ , the steerability vanishes, which can be attributed to decoherence effects [17].

## IV. RESULTS AND DISCUSSIONS

### A. Steady state

In the steady-state regime, the steerability between qubits  $A$  (Alice) and  $B$  (Bob) can manifest in different configurations depending on the sign of  $\Delta_{12}$ . For  $\Delta_{12} > 0$ , the system exhibits one-way steering, meaning either  $S_{A \rightarrow B} > 0$  and  $S_{B \rightarrow A} = 0$  (Alice can steer Bob but not vice versa), or  $S_{A \rightarrow B} = 0$  and  $S_{B \rightarrow A} > 0$  (the opposite situation). When  $\Delta_{12} = 0$ , the system allows either two-way steering ( $S_{A \rightarrow B} = S_{B \rightarrow A} > 0$ ) or no-way steering ( $S_{A \rightarrow B} = S_{B \rightarrow A} = 0$ ), the latter occurring even when the qubits remain entangled. In our model, the equalities in Equations (26) and (28) yield  $\Delta_{12} = 0$ , indicating a bidirectional steering symmetry between qubits  $A$  and  $B$  (see Figure 1(c)).

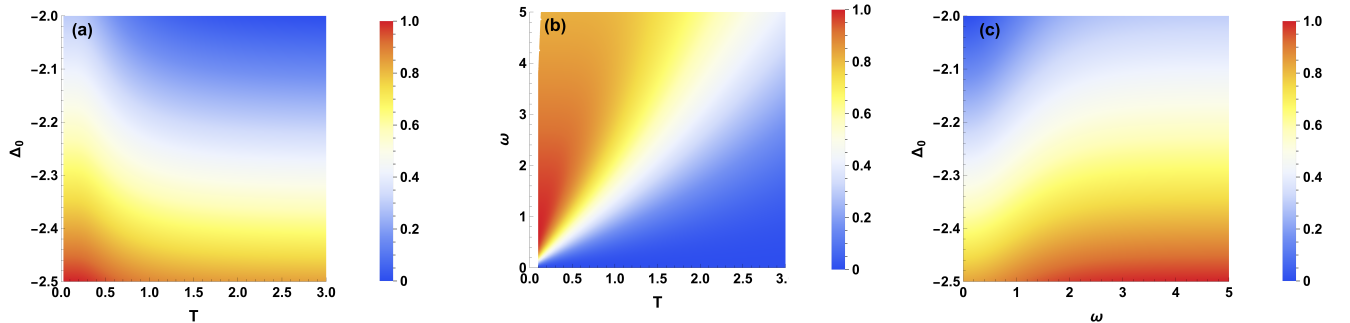


FIG. 2: (a) Quantum steering versus  $\Delta_0$  and  $T$  with  $\omega = 1$ ; (b) Quantum steering versus  $\omega$  and  $T$  with  $\Delta_0 = -2.2$ ; (c) Quantum steering versus  $\Delta_0$  and  $\omega$  with  $T = 0.8$ .

increases with increasing  $\Delta_0$ . At low temperatures, the steerability becomes larger for smaller values of  $\Delta_0$ . Nevertheless, higher the energy level spacing of the atom allow the steerability to persist over a broader temperature range.

In Fig. 1(c), we plot the steerabilities  $S_{A \rightarrow B}$ ,  $S_{B \rightarrow A}$ , along with the asymmetry  $\Delta_{12}$  as functions of the temperature  $T$ . We observe that  $S_{A \rightarrow B} = S_{B \rightarrow A} > 0$  (i.e.,  $\Delta_{12} = 0$ ) for  $T \in [0, 0.25]$ . This indicates the presence of two-way quantum steering between qubit A and qubit B. Moreover, for  $T \in [0.25, 1]$ , we have  $S_{A \rightarrow B} = S_{B \rightarrow A} = 0$ , effectively indicating negligible steering between the two qubits.

The three density plots in Fig. 2 illustrate how the quantum steering measure depends on the temperature  $T$  as well as on the parameters  $\Delta_0$  and  $\omega$ . The results show that quantum steering persists only within a limited low-temperature re-

gion, where quantum correlations remain sufficiently strong. As the temperature increases, thermal noise becomes progressively more dominant, acting as a strong source of decoherence that disrupts the quantum correlations. Consequently, the steering measure decreases continuously, since higher temperatures weaken the nonclassical features required to sustain directional correlations. When the thermal fluctuations become sufficiently strong, these correlations are effectively washed out, and quantum steering ceases to be observable in the high-temperature regime. The parameters  $\Delta_0$  and  $\omega$  play a central role in determining both the magnitude and the robustness of steering, as its variation modifies the structure of the density matrix and controls the extent of the region where steering survives. Overall, the three plots highlight the strong sensitivity of quantum steering to thermal fluctuations and the crucial role of  $\Delta_0$  and  $\omega$  in sustaining directional quantum correlations.

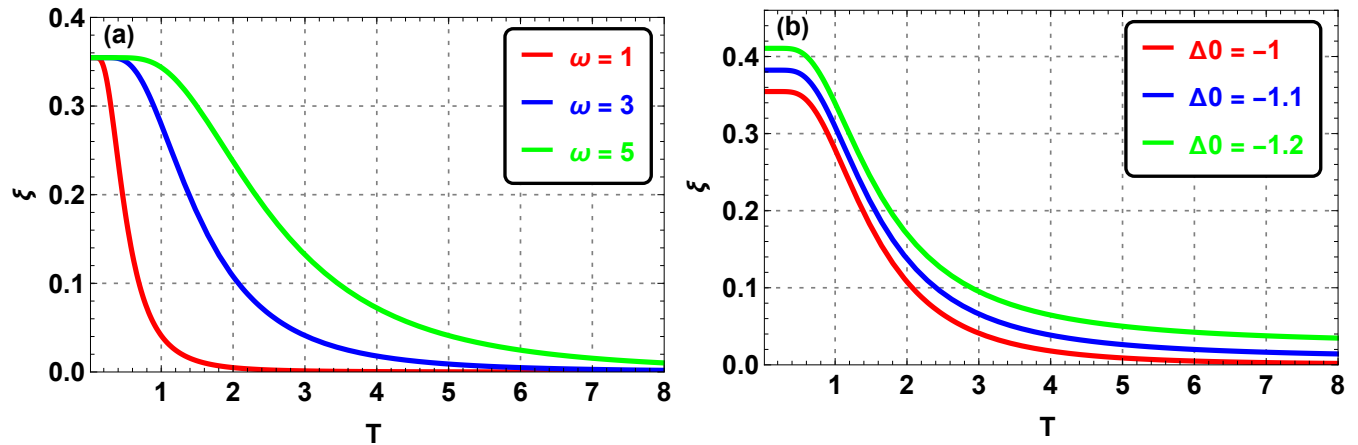


FIG. 3: (a) Entanglement of formation  $\xi$  versus temperature  $T$  for different values of  $\omega$  with  $\Delta_0 = -1$ ; (b) entanglement of formation versus  $T$  for different values of  $\Delta_0$  with  $\omega = 3$ .

The behavior of the entanglement of formation  $\xi$  as a function of temperature  $T$  for several values of  $\omega$  is examined in Fig. 3(a), with the initial state parameter fixed at  $\Delta_0 = -1$ . The results demonstrate that, as  $T \rightarrow 0$ , the entanglement reaches its maximum and becomes effectively independent of temperature. As expected, entanglement decreases monotonically with rising temperature due to thermal noise. Moreover, larger en-

ergy spacing  $\omega$  helps sustain higher entanglement values at finite temperatures, demonstrating that entanglement is more robust against thermal effects as  $\omega$  increases. These observations are consistent with the experimental findings on thermal entanglement reported in Refs. [83, 84].

In Fig. 3(b), we present the temperature dependence of the entanglement of formation  $\xi$  for different values of initial state

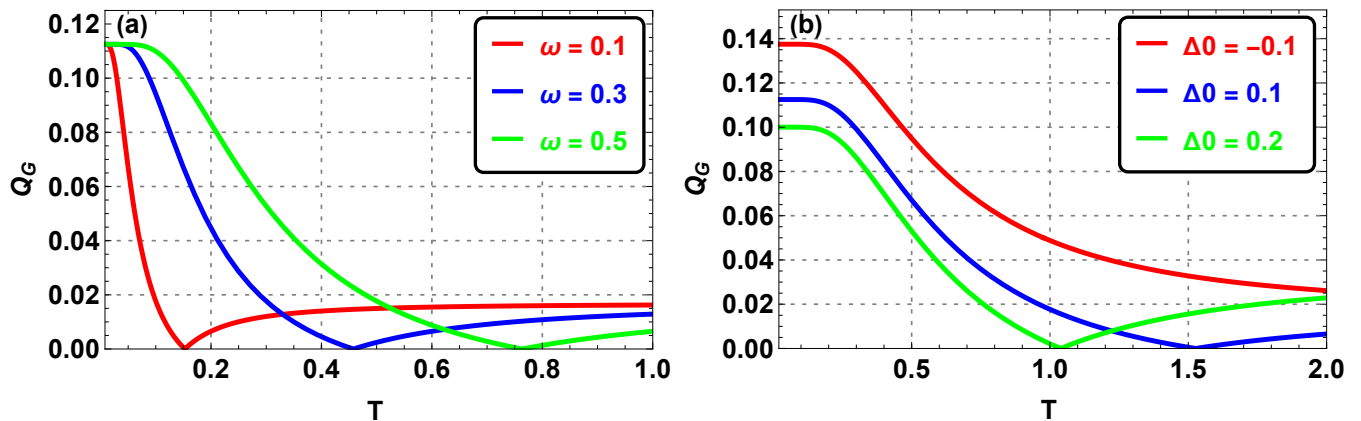
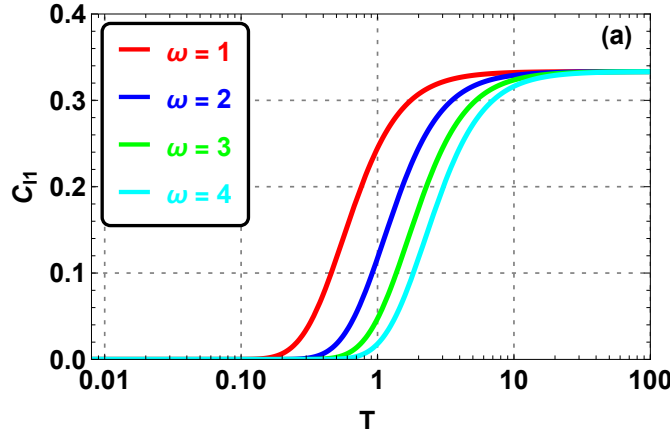


FIG. 4: Geometric quantum discord  $Q_G$  as a function of the temperature  $T$ ; (a) for different values of  $\omega$  with  $\Delta_0 = 0.1$ . (b) for different values of  $\Delta_0$  with  $\omega = 1$ .

parameter  $\Delta_0$ . Furthermore, the entanglement rapidly diminishes and tends to zero for sufficiently high values of  $T$ . Interestingly, in the intermediate temperature interval  $T \in [0, 0.4]$ , the entanglement increases as  $\Delta_0$  decreases, as illustrated in Fig. 3(b). For temperatures  $T > 5$ , the entanglement vanishes for different values of different values of  $\Delta_0$ .

In Fig. 4(a), The results show that the geometric quantum discord  $Q_G$  exhibits a non-monotonic behavior with temperature  $T$ : it initially decreases due to thermal fluctuations, then increases at higher temperatures. This behavior suggests that, despite the initial loss of correlations at low temperatures, certain thermal effects promote a partial restoration of quantum correlations at intermediate temperatures. The parameter  $\Delta_0$  sets the baseline correlation level, while the energy spacing  $\omega$



modulates the depth and position of the minimum in  $Q_G$ : larger values of  $\omega$  tend to mitigate the initial decay and enhance the persistence of quantum correlations.

The results in Fig. 4(b) indicate that the geometric quantum discord  $Q_G$  is highly sensitive to the initial state parameter  $\Delta_0$ . For all considered values of  $\Delta_0$ ,  $Q_G$  exhibits a non-monotonic behavior with temperature  $T$ , decreasing at low temperatures due to thermal fluctuations and then increasing at higher temperatures. The magnitude and position of the minimum of  $Q_G$  are strongly influenced by  $\Delta_0$ : larger values of  $\Delta_0$  lead to a higher baseline discord and a shallower initial decay, indicating that the choice of the initial state can enhance the robustness of quantum correlations against thermal effects. These observations emphasize the crucial role of the initial state configuration in shaping the thermal dynamics of quantum discord.

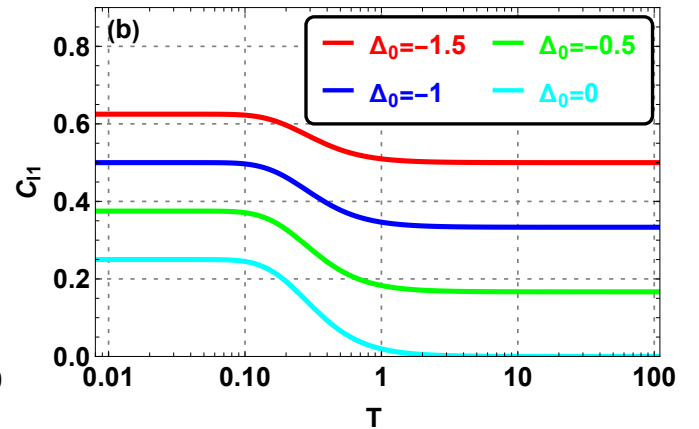


FIG. 5: The quantum coherence  $C_{l1}$  as a function of temperature  $T$  is presented: (a) for different values of the energy  $\omega$ , with initial state selection parameter  $\Delta_0 = 1$ ; (b) for different values of the initial state selection parameter  $\Delta_0$ , with  $\omega = 0.5$ .

The results in the figure 5(a) show that the quantum coherence  $C_{l1}$  increases with temperature  $T$ , approaching an asymptotic maximum value for all considered values of  $\omega$ . At low temperatures, the coherence is initially small, indicating limited quantum correlations. The energy spacing  $\omega$  affects the rate at which  $C_{l1}$  reaches its maximum: smaller values of  $\omega$  allow the coherence to saturate at lower temperatures, whereas larger  $\omega$  delay this saturation. These observations suggest that the energy separation plays a crucial role in determining the temperature scale over which quantum coherence.

Figure 5(b) illustrates the quantum coherence  $C_{l1}$  as a function of temperature  $T$  for various values of the parameter  $\Delta_0$ . The coherence generally decreases with increasing temperature, highlighting the suppressive effect of thermal fluctuations on quantum superpositions. At low temperatures ( $T \lesssim 0.1$ ),  $C_{l1}$  reaches its maximum values, indicating strong coherent superpositions between the qubit states. As the temperature increases, the coherence gradually diminishes, approaching lower values at high temperatures ( $T \sim 100$ ), where thermal noise dominates and superpositions are largely destroyed. Comparing different  $\Delta_0$  values, larger (less negative) interaction parameters

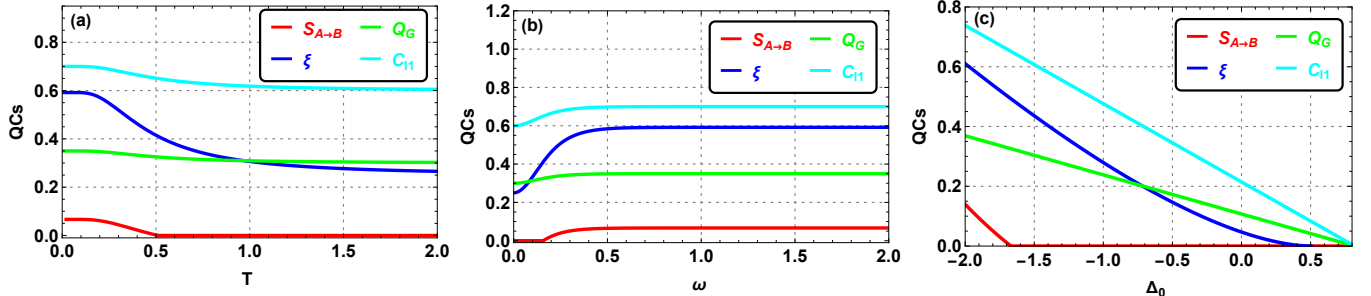


FIG. 6: Plot of quantum coherence ( $C_{l1}$ ) and quantum correlations, including quantum steering ( $S_{A \rightarrow B}$ ), entanglement of formation ( $\xi$ ), geometric quantum discord ( $Q_G$ ): (a) as a function of temperature ( $T$ ) with  $\Delta_0 = -1.8$  and  $\omega = 0.8$ ; (b) as a function of the energy ( $\omega$ ) at  $T = 0.1$  with  $\Delta_0 = -1.8$ ; and (c) as a function of ( $\Delta_0$ ) at  $T = 0.5$  with  $\omega = 1.5$ .

maintain higher coherence at low temperatures. In particular, the curve for  $\Delta_0 = -1.5$  exhibits the highest initial coherence, while more negative values ( $\Delta_0 = -1, -0.5, 0$ ) show progressively smaller coherence. This indicates that the interaction strength significantly affects the robustness of quantum coherence against thermal effects, emphasizing the role of tuning  $\Delta_0$  to preserve quantum superpositions in practical quantum systems.

Figures 6(a) and 6(b) jointly illustrate the influence of temperature and energy spacing on quantum coherence and quantum correlations in the system. As shown in Fig. 6(a), at low temperatures all quantifiers reach high values, revealing strong entanglement and robust nonclassical correlations. With increasing temperature, thermal fluctuations progressively degrade these resources, in accordance with the hierarchy of quantum correlations: quantum steering is the most fragile and disappears at moderate temperatures, whereas entanglement and quantum discord persist over a wider thermal range, and quantum coherence remains finite throughout. In contrast, Fig. 6(b) demonstrates that increasing the energy spacing parameter  $\omega$  enhances all quantum correlations, which rise rapidly for small  $\omega$  and then saturate beyond a critical value  $\omega \approx 0.5$ . This saturation marks an optimal regime where quantum resources are maximized and become insensitive to further increases in  $\omega$ , highlighting the complementary roles of temperature and

spectral tuning in controlling the robustness and optimization of quantum correlations.

As shown in Fig. 6(c), quantum coherence and all four quantum correlation measures decrease with increasing  $\Delta_0$ . While  $\xi$  and  $C_{II}$  remain relatively robust, steering ( $S_{A \rightarrow B}$ ) vanishes earlier, around  $\Delta_0 \approx -1.5$ , highlighting its fragility. All measures reach zero near  $\Delta_0 \approx 0.6$ , marking the transition to a classical state. This behavior identifies  $\Delta_0$  as an intrinsic decoherence parameter driving the progressive classicalization of the system. We remark also, that increasing the parameter  $\Delta_0$  gradually suppresses the more “fragile” and resourceful quantum correlations, such as steering (which is linked to nonlocality), while leaving the more fundamental and robust quantum features, like discord and coherence, largely unaffected, as these do not require strong nonlocal correlations.

## B. Dynamical state

In this section, we examine the dynamics of quantum resources in a UdW system subjected to correlated dephasing channels. We provide a detailed analysis of the influence of classical correlations, quantified by the parameter  $\mu$ , on the time evolution of quantum steering, entanglement, geometric quantum discord, and quantum coherence, in both Markovian and

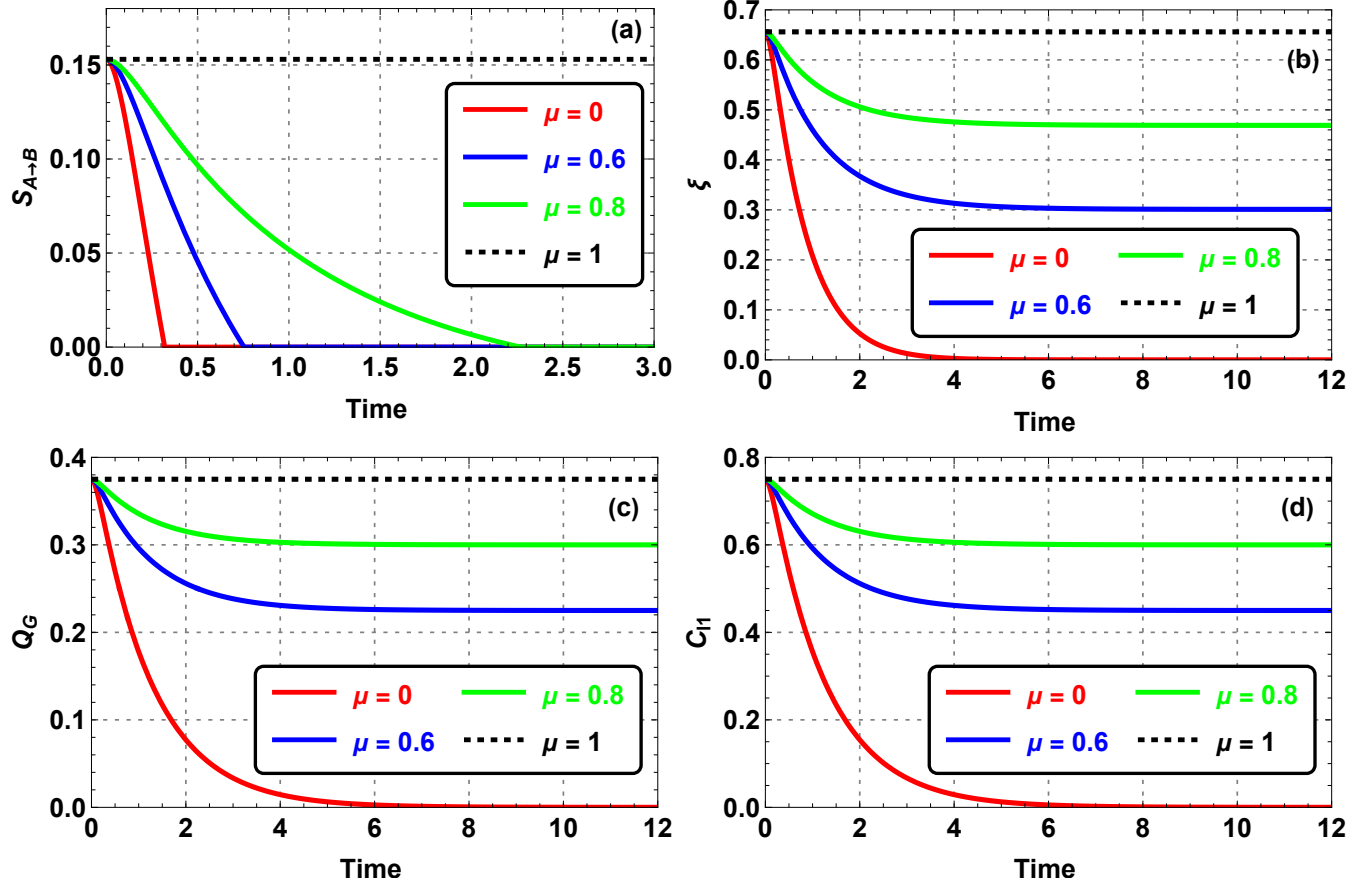


FIG. 7: Dynamical evolution of quantum steering  $S_{A \rightarrow B}$  (a), entanglement of formation  $\xi$  (b), geometric quantum discord  $Q_G$  (c), and quantum coherence  $C_{II}$  (d) in the Markovian regime with  $\tau = 0.1$ ,  $T = 0.1$ ,  $\Delta_0 = -2$ , and  $\omega = 1$ . For all curves, the red, blue, green, and black curves correspond to  $\mu = 0, 0.6, 0.8$ , and  $1$ , respectively.

non-Markovian regimes. Our results reveal a significant enhancement of these quantum resources as the degree of classical correlations increases.

Starting from the thermal time-dependent state given in Equation (24), analytical expressions for quantum steering, entanglement, geometric quantum discord, and quantum coherence are obtained by substituting  $\rho_{23}$  with  $\zeta\rho_{23}$ , respectively, in Equations (26), (31), (36), and (41), where  $\zeta(t) = (1 - \mu)h^2(t) + \mu$ . The results displayed in Figure 7 demonstrate the crucial role played by classical correlations in enhancing quantum resources within a Markovian environment. Increasing  $\mu$  yields a

marked improvement in quantum steering, entanglement, geometric quantum discord, and quantum coherence. For  $\mu < 1$ , these quantities decay monotonically and exponentially over time, indicating that weaker classical correlations amplify decoherence effects. In particular, when  $\mu = 0$ , Equation (23) reduces to  $\zeta(t) = h^2(t)$ , and all quantum resources rapidly decay toward their steady-state values. In contrast, for a fully correlated dephasing channel ( $\mu = 1$ ), all quantifiers remain constant, reflecting complete robustness against decoherence. These findings highlight the importance of classical correlations in preserving quantum coherence and improving the performance of quantum systems in information-processing tasks.

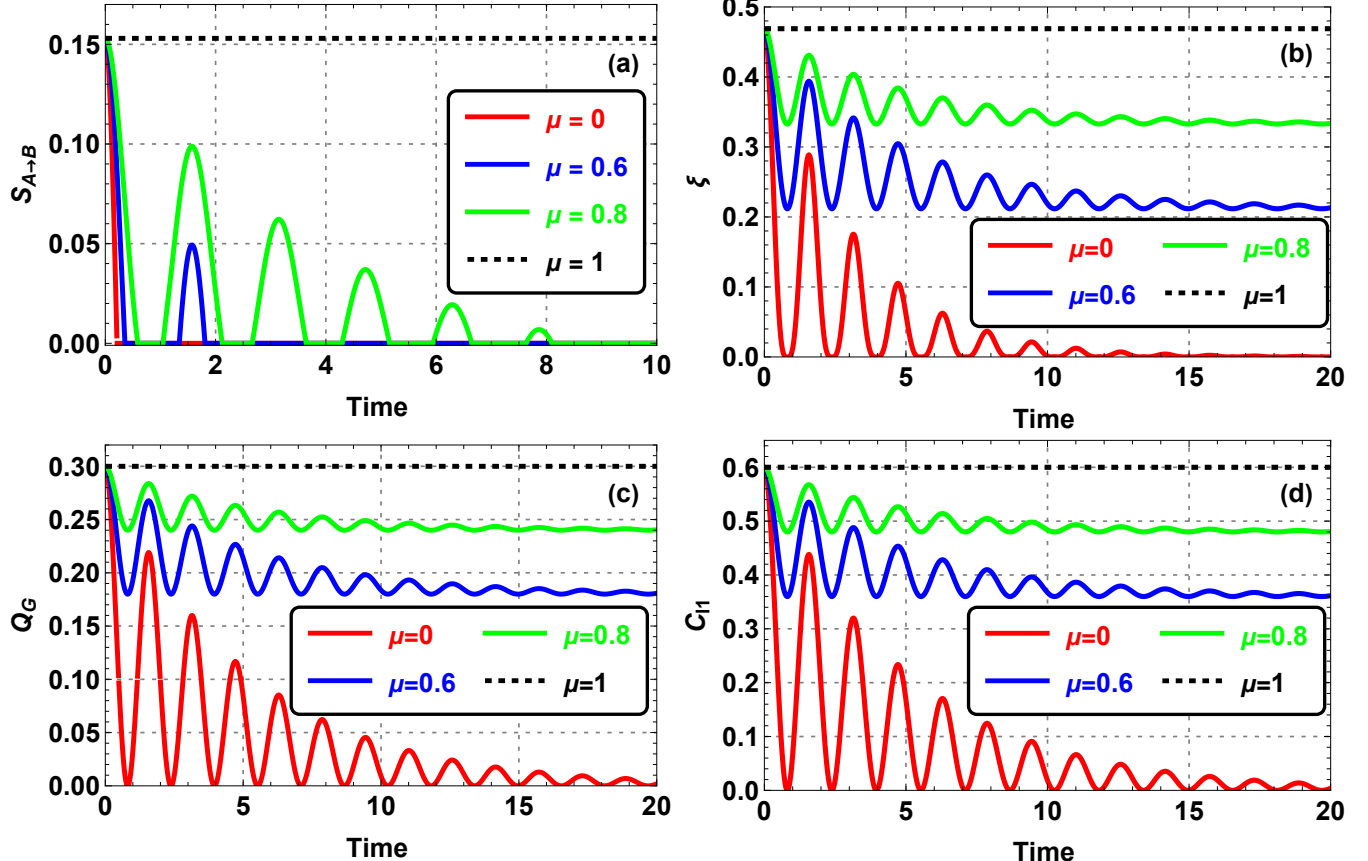


FIG. 8: Time evolution of quantum steering  $S_{A \rightarrow B}$  (a), entanglement of formation  $\xi$  (b), geometric quantum discord  $Q_G$  (c), and quantum coherence  $C_{11}$  (d) in the Non-Markovian regime with  $\tau = 5$ ,  $T = 0.1$ ,  $\Delta_0 = -2$ , and  $\omega = 1$ . For all curves, the red, blue, green, and black curves correspond to  $\mu = 0, 0.6, 0.8$ , and  $1$ , respectively.

Figure 8 extends the analysis to the non-Markovian regime. This figure shows that, for all values  $\mu < 1$ , the quantum resources quickly decay to zero, whereas for  $\mu = 1$ , they remain constant in time. For  $\mu < 1$ , all quantities display oscillatory behavior due to non-Markovian memory effects, with the amplitude of the oscillations gradually decreasing over time, as depicted in Figures 8(a-d).

As shown in Figure 9(a), the temporal evolution of quantum steering, entanglement, geometric quantum discord, and quantum coherence is examined in the Markovian regime. The hierarchy among these quantifiers remains unchanged throughout the evolution, following the ordering: coherence  $\supseteq$

geometric quantum discord  $\supseteq$  entanglement  $\supseteq$  steerability.

This demonstrates that the UdW may remain entangled even when steerability vanishes, and more generally, that entanglement does not necessarily imply steerability. In contrast, the geometric quantum discord ( $Q_G$ ) and the coherence ( $C_{11}$ ) prove to be the most robust, maintaining nonzero values well beyond the disappearance of steering and entanglement. This contrast highlights that the system retains its fundamental quantum character—namely, superposition and general nonclassical correlations—even after losing the resources that are most valuable for quantum communication and information-processing protocols, such as nonlocality and steerability.

Figure 9(b) displays the evolution of the same correlations in the non-Markovian regime. A similar general behavior is observed; however, in this case, the correlations evolve sinusoidally and in phase, with oscillations whose amplitude gradually decreases. This indicates that non-Markovian memory ef-

fects play a significant role in shaping the dynamics of quantum correlations, leading to more coherent and periodic behavior compared to the Markovian regime, which is dominated by stronger decoherence processes.

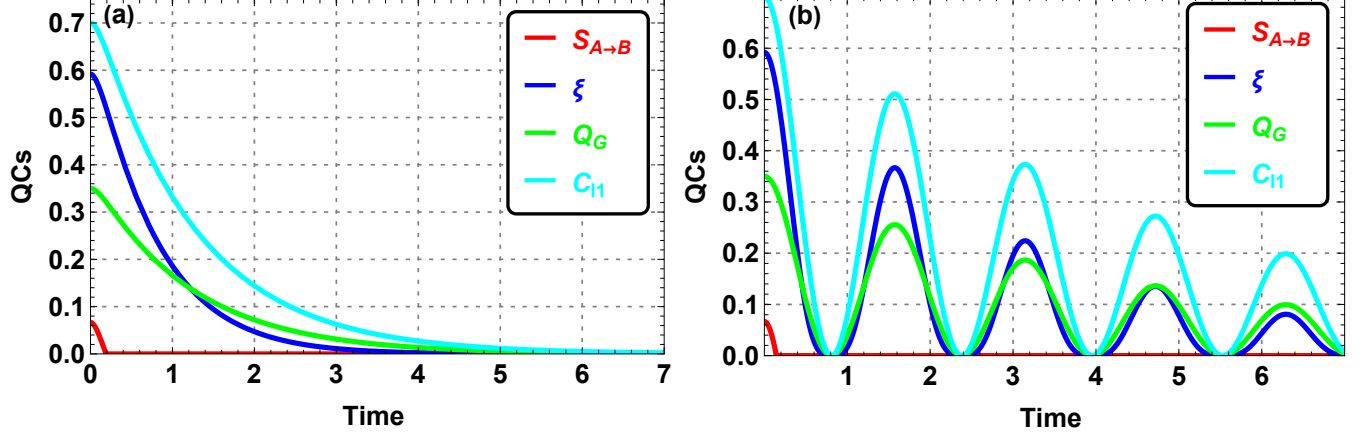


FIG. 9: Comparison of quantum steering, entanglement of formation, geometric quantum discord, and quantum coherence in (a) the Markovian regime with  $\tau = 0.1$  and (b) the non-Markovian regime with  $\tau = 5$ . The fixed parameters are  $\Delta_0 = -2$ ,  $\omega = 3$ ,  $\mu = 0$ , and  $T = 0.2$ .

## V. QUANTUM THERMODYNAMICS

The eigenvalues of  $\rho_{AB}$  are straightforwardly obtained as

$$\lambda_1 = \rho_{11}, \quad \lambda_2 = \rho_{22}, \quad \lambda_3 = \rho_{22} + \rho_{23}, \quad \lambda_4 = \rho_{22} - \rho_{23}, \quad (42)$$

which satisfy  $\sum_{k=1}^4 \lambda_k = 1$ .

Hence, the von Neumann entropy is given by [85]

$$S = - \sum_{k=1}^4 \lambda_k \ln \lambda_k. \quad (43)$$

The internal energy is then defined by

$$U = \text{tr} [H_{\text{eff}} \rho_{AB}], \quad (44)$$

in the weak-coupling limit, the internal energy simplifies to

$$U = \omega (\rho_{11} - \rho_{22}). \quad (45)$$

The quantum Stirling cycle (QSC) consists of four successive thermodynamic stages—two quantum isothermal processes and two isochoric processes, as illustrated in Figure 10—where, during the isothermal transformations, the system remains in thermal equilibrium with a heat reservoir while the characteristic energy parameter ( $\omega$ ) is varied, and in the isochoric stages, the system exchanges heat with the baths while  $\omega$  remains constant; the four stages are described as follows [86, 87]

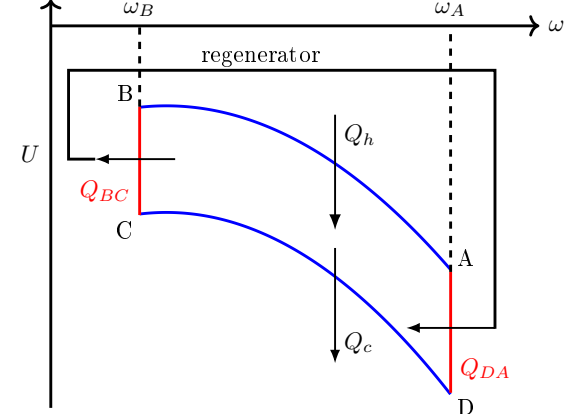


FIG. 10: The diagram of the Stirling cycle [31], where  $Q_h$  denotes the absorbed heat,  $Q_c$  the released heat,  $T_h$  the hot-bath temperature, and  $T_c$  the cold-bath temperature.

**A→B (Isothermal expansion):** The working substance interacts with a hot thermal bath at temperature  $T_h$ , while the energy parameter varies from. During this process, the system exchanges heat with the reservoir, which can be expressed as

$$Q_{AB} = T_h \int_A^B dS = T_h (S_B - S_A), \quad (46)$$

where the entropy  $S$  is determined from Eq. (43).

**B→C (Isochoric cooling):** The energy parameter  $\omega$  remains constant at  $\omega = \omega_B$ , while the temperature decreases from  $T_h$  to  $T_c$ . The exchanged heat is given by

$$Q_{BC} = U_c - U_B = U(\omega_B, T_c) - U(\omega_B, T_h), \quad (47)$$

where  $U$  denotes the internal energy of the system.

**C→D (Isothermal compression):** The energy parameter  $\omega$  is reduced from  $\omega_B$  to  $\omega_A$ , while the temperature is maintained at  $T_c$ . The exchanged heat during this step is

$$Q_{CD} = T_c \int_C^D dS = T_c(S_D - S_C). \quad (48)$$

**D→A (Isochoric heating):** The energy parameter remains constant at  $\omega = \omega_A$ , while the temperature increases from  $T_c$  to  $T_h$ . The absorbed heat is expressed as

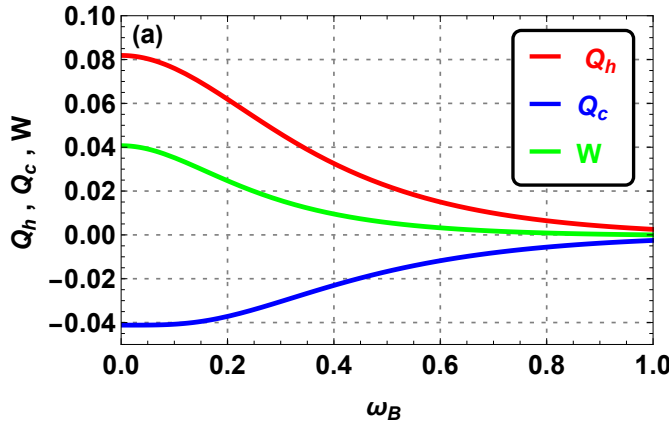
$$Q_{DA} = U_A - U_D = U(\omega_A, T_h) - U(\omega_A, T_c). \quad (49)$$

Over a complete cycle, the total absorbed and released heats are given by

$$Q_h = Q_{AB} + Q_{DA}, \quad Q_c = Q_{BC} + Q_{CD}, \quad (50)$$

where  $Q_{AB}$  and  $Q_{CD}$  correspond to the input and output heats, respectively. The total work performed by the system is

$$W = Q_{AB} + Q_{BC} + Q_{CD} + Q_{DA}, \quad (51)$$



and the efficiency  $\eta$  of the quantum heat engine is expressed as

$$\eta = \frac{W}{Q_h}. \quad (52)$$

### A. Steady state

Figure 11(a) presents the behavior of the absorbed heat ( $Q_h$ ), the released heat ( $Q_c$ ), and the work output ( $W$ ) as functions of  $\omega_B$ , for  $\omega_A = 1$ ,  $T_h = 2T_c$ , and  $\Delta_0 = -1.5$ . This figure shows that when  $\omega_B$  is varied from 0 to 1, both  $Q_h$  and  $W$  maintain positive values. Conversely,  $Q_c$  remains negative within the interval  $0 < \omega_B < 0.9$ . This sign convention confirms that the system operates as a heat engine in this specific regime.

Figure 11(b) shows the efficiency ( $\eta$ ) of the engine as a function of the energy spacing ( $\omega_B$ ) for different initial spacings ( $\omega_A$ ). The efficiency decreases as  $\omega_B$  increases. This indicates that a larger energy spacing during the cold stroke reduces the work output relative to the heat absorbed during the hot stroke, consequently lowering the conversion efficiency. The rate of decrease depends on  $\omega_A$ : higher initial spacings correspond to a smaller efficiency loss for the same increase in  $\omega_B$ . In all cases, the efficiency remains below the Carnot limit  $\eta_c = 1 - T_c/T_h$ ,

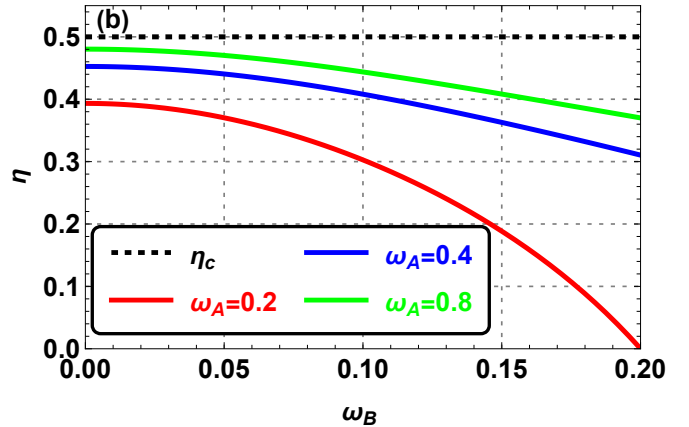


FIG. 11: Variation of  $Q_h$ ,  $Q_c$ , the work done  $W$  (a) and the efficiency  $\eta$  (b) versus  $\omega_B$  with  $\Delta_0 = -1.5$ ,  $T_h = 2T_c$ , and  $\omega_A = 1$

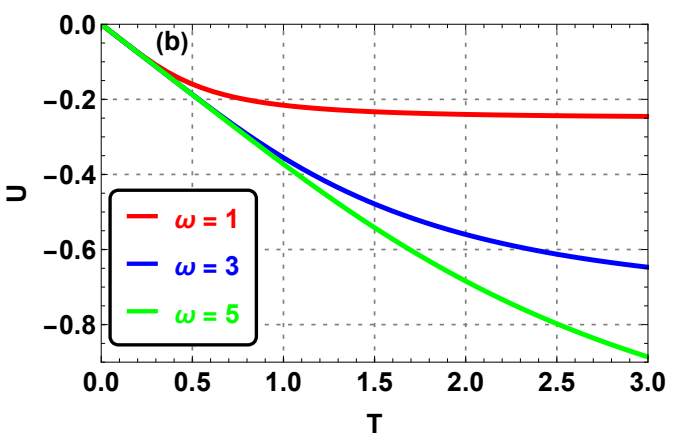
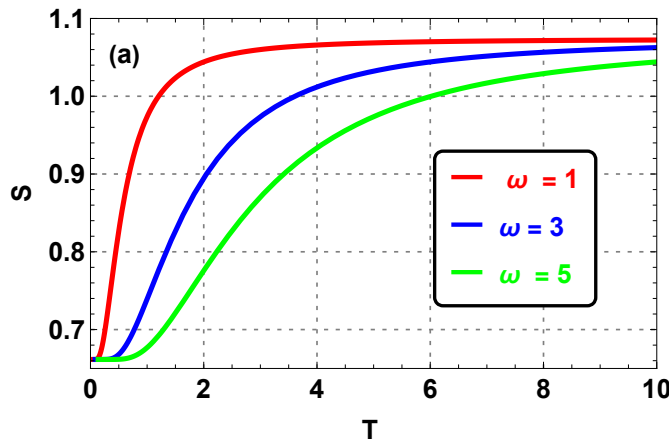
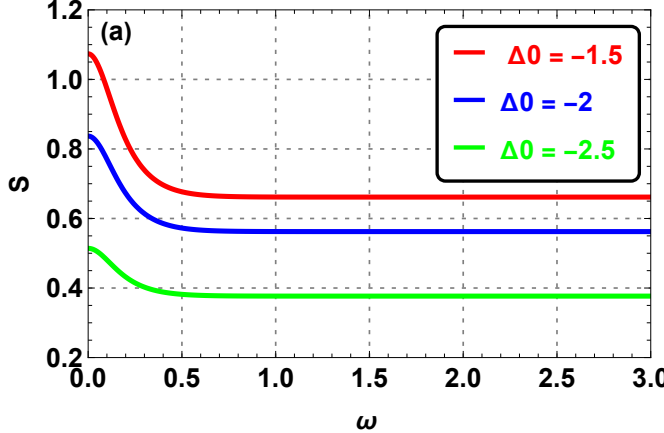


FIG. 12: Variation of the (a) entropy, (b) internal energy versus  $T$  for different values of the energy  $\omega$  with  $\Delta_0 = -1.5$

as expected for an irreversible cycle. In summary, the figure illustrates that increasing the energy spacing in the cold branch negatively affects the engine performance, highlighting the sensitivity of quantum engines to the tuning of energy-level spacings.

Figure 12(b) illustrates the behavior of the internal energy



( $U$ ) as a function of the bath temperature ( $T$ ) for different values of spacing ( $\omega$ ). For all values of  $\omega$ , the internal energy remains negative and decreases monotonically with temperature. Overall, the figure shows that both  $T$  and  $\omega$  strongly influence the energetic response of the system, with lower energy spacing producing deeper negative internal-energy values.

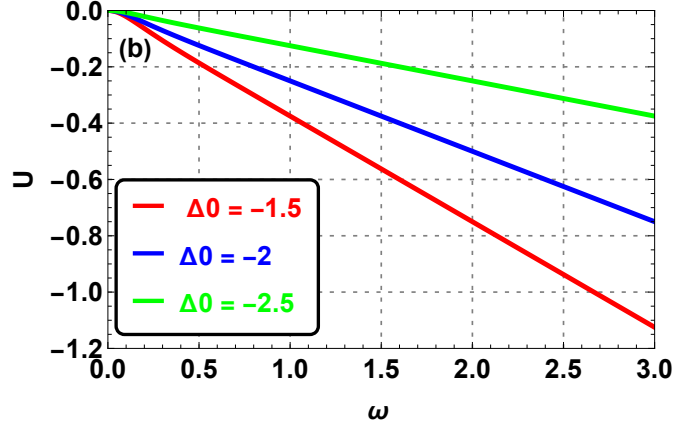
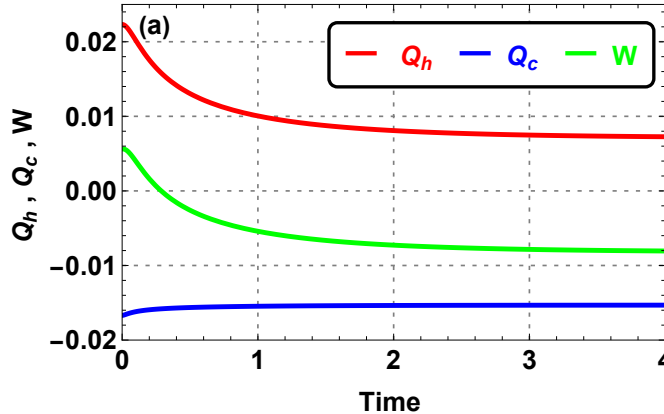


FIG. 13: Variation of the (a) entropy, (b) internal energy versus  $\omega$  for different values of the initial state parameter  $\Delta_0$  with  $T = 0.1$ .

The behavior of the von Neumann entropy ( $S$ ) as a function of the energy spacing ( $\omega$ ) for various values of the initial state parameter ( $\Delta_0$ ) is shown in Figure 13(a). The entropy decreases rapidly for  $\omega \lesssim 0.4$ , indicating a fast reduction in the quantum mixedness of the system, and then remains nearly constant for  $\omega \gtrsim 0.5$ . Furthermore, larger absolute values of  $\Delta_0$  correspond to generally lower entropy, demonstrating that the initial state parameter strongly affects the degree of quantum uncertainty. These results highlight the combined influence of the initial state configuration and energy spacing on the system's quantum correlations and thermal properties.

Figure 13(b) illustrates the behavior of the internal energy  $U$



as a function of the energy spacing  $\omega$  for different values of the initial state parameter  $\Delta_0$  at a fixed temperature  $T = 0.1$ . For all considered values of  $\Delta_0$ , the internal energy is negative and decreases linearly with  $\omega$ . Furthermore, larger absolute values of  $\Delta_0$  correspond to generally higher internal energy, demonstrating that the initial state strongly affects the system's energy content. These results highlight the combined effect of the initial state configuration and energy spacing on the thermodynamic properties of the system at this temperature.

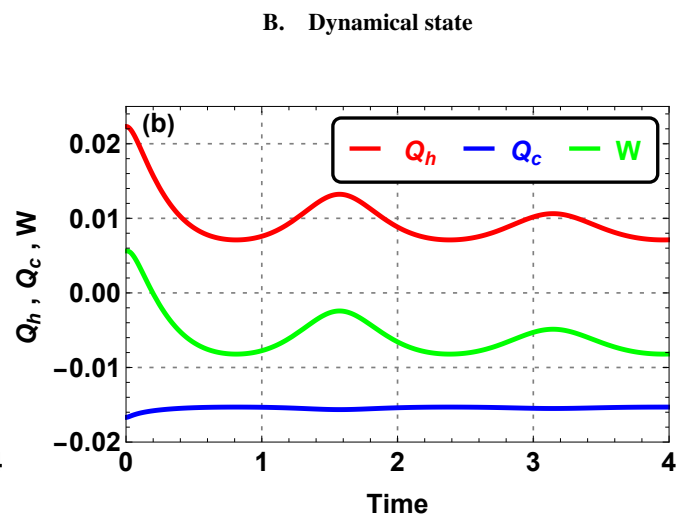


FIG. 14: Comparison of  $Q_h$ ,  $Q_c$ , the work done  $W$  in (a) the Markovian regime with  $\tau = 0.1$  and (b) the non-Markovian regime with  $\tau = 5$ . The fixed parameters are  $\Delta_0 = -1.5$ ,  $\omega_A = 1$ ,  $\omega_B = 0.5$ ,  $\mu = 0.4$ , and  $T_h = 2T_c$ .

Figure 14 compares the heat exchanged with the hot bath ( $Q_h$ ), the heat released to the cold bath ( $Q_c$ ), and the extracted work ( $W$ ) as functions of time in the Markovian ( $\tau = 0.1$ ) and

non-Markovian ( $\tau = 5$ ) regimes. In the Markovian case, all quantities evolve monotonically toward their steady values, indicating a smooth, irreversible relaxation. In contrast, the non-

Markovian dynamics exhibits pronounced oscillations in  $Q_h$ ,  $Q_c$ , and  $W$ , reflecting memory-induced backflow of information and energy between the working substance and the reservoir. These oscillations enhance the instantaneous work output

but delay the stabilization of the thermodynamic cycle. Overall, the figure demonstrates that non-Markovian memory effects significantly modify the energetic exchanges and transient work production of the quantum heat engine.

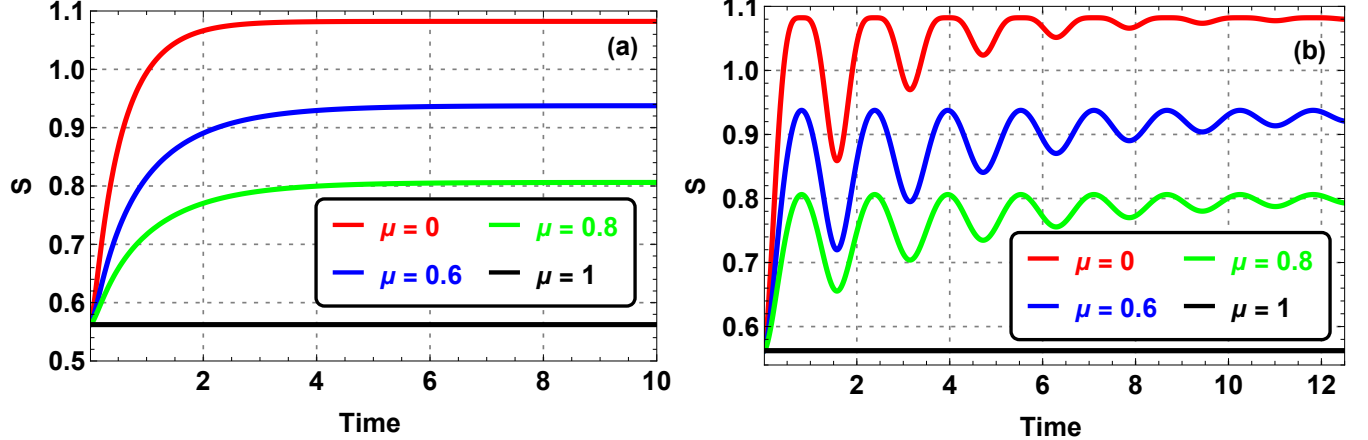


FIG. 15: Comparison of the entropy ( $S$ ) in (a) the Markovian regime ( $\tau = 0.1$ ) and (b) the non-Markovian regime ( $\tau = 5$ ) for different values of the classical correlation parameter ( $\mu$ ). The fixed parameters are  $\Delta_0 = -2$ ,  $\omega = 2$ , and  $T = 0.1$ .

Figure 15 compares the time evolution of the von Neumann entropy  $S$  for different values of the classical correlation parameter  $\mu$  in both (a) the Markovian regime ( $\tau = 0.1$ ) and (b) the non-Markovian regime ( $\tau = 5$ ). In the Markovian case, the entropy increases monotonically to achieve its steady-state, it is

observed that the entropy grows over time, whereas increasing values of  $\mu$  lead to a reduction in entropy.

In contrast, the non-Markovian regime exhibits pronounced oscillations reflecting memory effects. Although the amplitude of these revivals becomes more significant as  $\mu$  decreases, it gradually decreases over time.

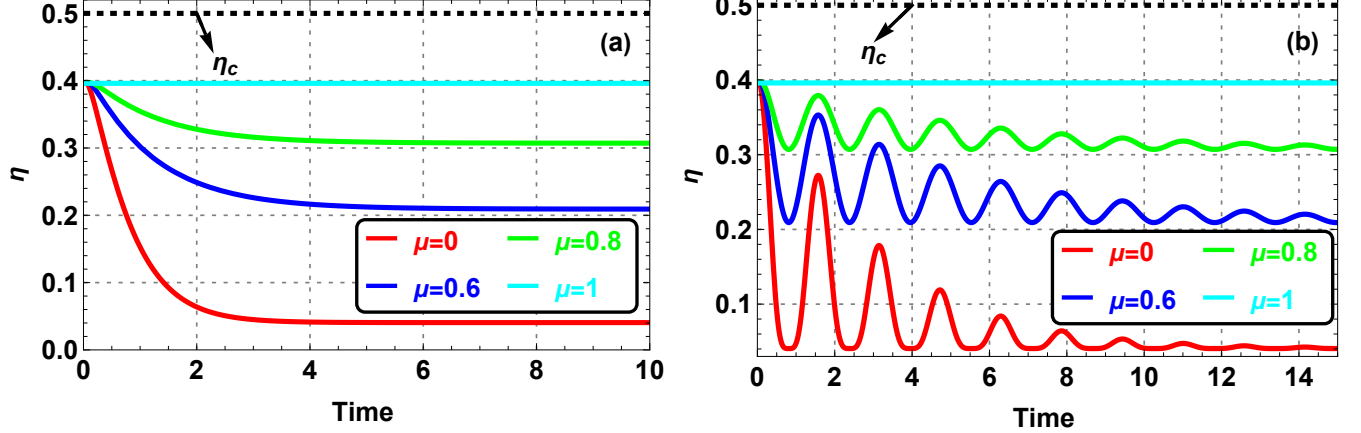


FIG. 16: Comparison of the efficiency ( $\eta$ ) in (a) the Markovian regime ( $\tau = 0.1$ ) and (b) the non-Markovian regime ( $\tau = 5$ ) for different values of the classical correlation parameter ( $\mu$ ). The fixed parameters are  $\Delta_0 = -1.5$ ,  $\omega_A = 1$ ,  $\omega_B = 0.5$ , and  $T_h = 2T_c$ .

Figure 16 compares the efficiency ( $\eta$ ) of the quantum heat engine in the (a) Markovian regime ( $\tau = 0.1$ ) and (b) non-Markovian regime ( $\tau = 5$ ) across several values of the classical correlation parameter ( $\mu$ ). In both regimes, the efficiency increases with stronger classical correlations ( $\mu$ ), indicating that such correlations enhance the engine's performance. However, the efficiency gradually decreases over time in both regimes. In

the non-Markovian regime ( $\tau = 5$ ), more pronounced oscillations and a higher peak efficiency are observed. These oscillations reflect the backflow of information that helps preserve quantum coherence during the cycle, although their amplitude gradually decreases over time. Overall, memory effects significantly improve the engine's performance compared to the pure Markovian regime ( $\tau = 0.1$ ).

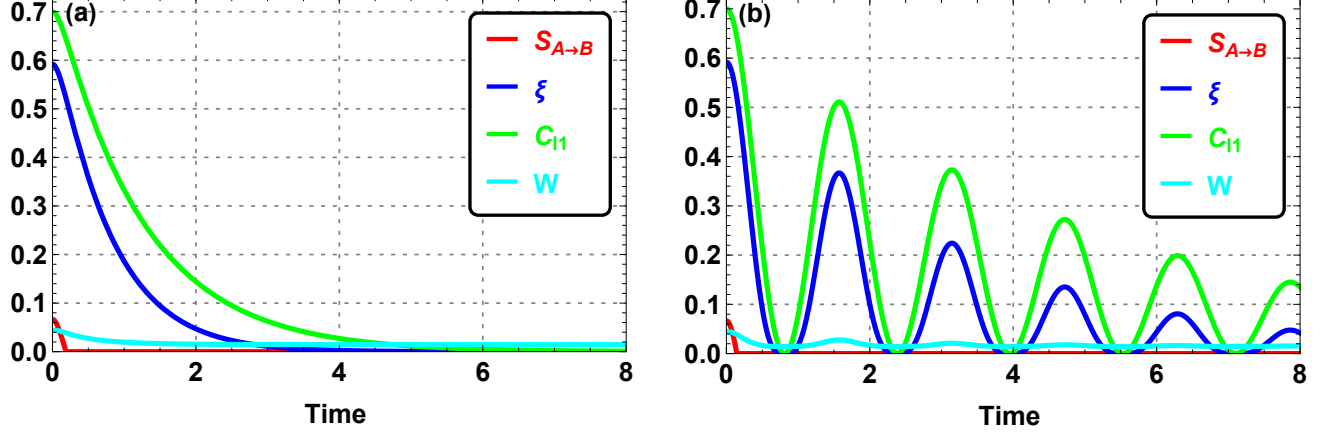


FIG. 17: Comparison of quantum steering, entanglement of formation, quantum coherence, and the work done in (a) the Markovian regime with  $\tau = 0.1$  and in (b) the non-Markovian regime with  $\tau = 5$ . The fixed parameters are  $\Delta_0 = -1.8$ ,  $\omega = 3$ ,  $\mu = 0$ ,  $T = 0.2$ ,  $\omega_A = 2$ ,  $\omega_B = 0.5$  and  $T_h = 1.5T_c$ .

As illustrated in Figure 17, the time evolution of quantum steering ( $S_{A \rightarrow B}$ ), entanglement ( $\xi$ ), quantum coherence ( $C_{l1}$ ), and the extracted work ( $W$ ) is analyzed for both the Markovian ( $\tau = 0.1$ ) and non-Markovian ( $\tau = 5$ ) regimes. In the Markovian regime, steering rapidly vanishes, the work remains relatively weak, entanglement gradually decreases, and quantum coherence persists longer before fading. In the non-Markovian regime, more pronounced oscillations are observed for all quantities, reflecting memory effects and information backflow, yet their amplitude also gradually decreases over time. We observe that an increase in coherence results in a higher amount of extracted work. Conversely, the extracted work decreases as the bath temperature rises. Moreover, for  $t \gtrsim 4$ , these quantities gradually vanish over time due to the influence of the environment. Figure 17 shows that the extracted work, quantum steering and entanglement are bounded by coherence. Moreover, entanglement and coherence, as quantum resources, are beneficial for work extraction.

## VI. CONCLUSION

In this work, we have explored the intricate relationship between quantum correlations, quantum coherence and quantum thermodynamics in a quantum heat engine modeled by Unruh-DeWitt detectors. By examining both the steady and dynam-

ical states of quantum resources—such as entanglement, geometric quantum discord, and coherence—we showed that their evolution is profoundly influenced by the characteristics of the surrounding environment. In particular, we analyzed the behavior of coherence and various forms of quantum correlations with respect to the temperature ( $T$ ), the energy spacing ( $\omega$ ), and the initial state parameter ( $\Delta_0$ ). This allowed us to compare not only coherence with different measures of quantum correlations, but also the interplay between these quantum resources and the thermodynamic performance of the engine. Our analysis reveals that non-Markovian memory effects play a constructive role: they mitigate the degradation of quantum resources and enhance key thermodynamic quantities, including heat exchange, work extraction, and overall engine efficiency. These findings underscore the central importance of both quantum and classical correlations in determining the operational performance of quantum thermal devices. Beyond providing deeper insight into the connections between quantum information and thermodynamics, our study highlights practical avenues for optimizing quantum technologies operating in relativistic or open-system regimes. Future research may extend this framework to multipartite systems, more general detector trajectories, or strong-coupling regimes, potentially uncovering additional mechanisms through which environmental memory and quantum resources can be harnessed to boost the performance of quantum machines.

---

[1] A. Einstein, B. Podolsky, and N. Rosen, *Phys. Rev.* **47**, 777 (1935).  
[2] E. Schrödinger, *Proceedings of the Cambridge Philosophical Society* **31**, 553 (1935).  
[3] J. S. Bell, *Physics Physique Fizika* **1**, 195 (1964).  
[4] H. M. Wiseman, S. J. Jones, and A. C. Doherty, *Phys. Rev. Lett.* **98**, 140402 (2007).  
[5] R. Uola, A. C. S. Costa, X. Ni, and O. Gühne, *Rev. Mod. Phys.* **92**, 015001 (2020).  
[6] X. Ma, A. Qarry, J. Kofler, T. Jennewein, and A. Zeilinger, *Phys. Rev. A* **79**, 042101 (2009).  
[7] J. Schneeloch, C. J. Broadbent, S. P. Walborn, E. G. Cavalcanti, and J. C. Howell, *Phys. Rev. A* **87**, 062103 (2013).  
[8] A. Ferraro, L. Aolita, D. Cavalcanti, F. M. Cucchietti, and A. Acín, *Physical Review A* **81**, 052318 (2010).  
[9] K. Modi, A. Brodutch, H. Cable, T. Paterek, and V. Vedral, *Reviews of Modern Physics* **84**, 1655 (2012).

[10] B. Dakic, V. Vedral, and C. Brukner, *Physical Review Letters* **105**, 190502 (2010).

[11] M. L. Hu, X. Hu, J. Wang, Y. Peng, Y. R. Zhang, and H. Fan, *Physics Reports* **762**, 1 (2018).

[12] C. Cruz, M. Anka, M. Reis, R. Bachelard, and A. Santos, *Quantum Science and Technology* **7**, 025020 (2022).

[13] A. Zeilinger, *Physica Scripta* **T76**, 203 (1998).

[14] A. Zeilinger, *Physica Scripta* **92**, 072501 (2017).

[15] R. J. Glauber, *Physical Review* **131**, 2766 (1963).

[16] E. C. G. Sudarshan, *Physical Review Letters* **10**, 277 (1963).

[17] W. H. Zurek, *Reviews of Modern Physics* **75**, 715 (2003).

[18] P. Kammerlander and J. Anders, *Scientific Reports* **6**, 22174 (2016).

[19] K. Zhang, X. Wang, Q. Zeng, and J. Wang, *PRX Quantum* **3**, 030315 (2022).

[20] C. Filgueiras, O. Rojas, and M. Rojas, *Annalen der Physik* **532**, 2000207 (2020).

[21] K. Berrada, *Physica E* **116**, 113784 (2020).

[22] M. H. Partovi, *Physics Letters A* **137**, 440 (1989).

[23] J. Gemmer, M. Michel, and G. Mahler, *Quantum Thermodynamics* (Springer, New York, 2009).

[24] C. A. Utreras-Díaz and D. Laroze, *Physica B* **476**, 77 (2015).

[25] J. Roßnagel, O. Abah, F. Schmidt-Kaler, K. Singer, and E. Lutz, *Physical Review Letters* **112**, 030602 (2014).

[26] H. T. Quan, Y.-X. Liu, C. P. Sun, and F. Nori, *Physical Review E* **76**, 031105 (2007).

[27] E. Aydiner and S. D. Han, *Physica A* **509**, 766 (2018).

[28] C. Cruz, D. O. Soares-Pinto, P. Brandao, A. M. dos Santos, and M. S. Reis, *Europhysics Letters* **113**, 40004 (2016).

[29] H. Wang, S. Liu, and J. He, *Physical Review E* **79**, 041113 (2009).

[30] G. Watanabe, B. P. Venkatesh, and P. Talkner, *New Journal of Physics* **22**, 013055 (2020).

[31] X. L. Huang, X. Y. Niu, X. M. Xiu, and X. X. Yi, *European Physical Journal D* **68**, 32 (2014).

[32] S. Cakmak, F. Turkpence, and F. Altintas, *European Physical Journal Plus* **132**, 554 (2017).

[33] S. H. Su, C. P. Sun, S. W. Li, and J. C. Chen, *Physical Review E* **93**, 052103 (2016).

[34] S. Carnot, *Réflexions sur la Puissance Motrice du Feu et sur les Machines propres à Développer cette Puissance* (Bachelier, Paris, 1824).

[35] R. Kosloff and A. Levy, *Annual Review of Physical Chemistry* **65**, 365 (2014).

[36] T. Feldmann and R. Kosloff, *Physical Review E* **70**, 046110 (2004).

[37] Y. Rezek and R. Kosloff, *New Journal of Physics* **8**, 83 (2006).

[38] B. Lin and J. Chen, *Physical Review E* **67**, 046105 (2003).

[39] A. Insinga, B. Andresen, and P. Salamon, *Physical Review E* **94**, 012119 (2016).

[40] R. Kosloff and Y. Rezek, *Entropy* **19**, 136 (2017).

[41] E. O. Oladimeji, *Physica E* **111**, 113 (2019).

[42] E. O. Oladimeji, S. Owolabi, and J. Adeleke, *Chinese Journal of Physics* **70**, 151 (2021).

[43] M. O. Scully, *Physical Review Letters* **88**, 050602 (2002).

[44] J. Wang, Y. Ma, and J. He, *Europhysics Letters* **111**, 20006 (2015).

[45] X. L. Huang, H. Xu, X. Y. Niu, and Y. D. Fu, *Physica Scripta* **88**, 065008 (2013).

[46] H. P. Peng, M. F. Fang, and C. Y. Zhang, *International Journal of Theoretical Physics* **58**, 1651 (2019).

[47] T. D. Kieu, *Physical Review Letters* **93**, 140403 (2004).

[48] H. T. Quan, P. Zhang, and C. P. Sun, *Physical Review E* **72**, 056110 (2005).

[49] J. H. Wang, Z. Q. Wu, and J. Z. He, *Physical Review E* **85**, 041148 (2012).

[50] M. Josefsson, A. Svilans, A. M. Burke, E. A. Hoffmann, S. Fahlvik, C. Thelander, M. Leijnse, and H. Linke, *Nature Nanotechnology* **13**, 920 (2018).

[51] Y. S. Liu, X. F. Yang, X. K. Hong, M. S. Si, F. Chi, and Y. Guo, *Applied Physics Letters* **103**, 093901 (2013).

[52] J. Z. He, X. He, and J. Zheng, *Chinese Physics B* **21**, 050303 (2012).

[53] A. H. Bahamin Pili, R. Khordad, and H. R. Rastegar Sedehi, *European Physical Journal Plus* **138**, 871 (2023).

[54] A. H. Bahamin Pili, R. Khordad, H. R. Rastegar Sedehi, and A. Avazpour, *International Journal of Theoretical Physics* **62**, 192 (2023).

[55] S. A. Fulling, *Physical Review D* **7**, 2850 (1973).

[56] P. C. W. Davies, *Journal of Physics A: Mathematical and General* **8**, 609 (1975).

[57] W. G. Unruh, *Physical Review D* **14**, 870 (1976).

[58] F. Benatti and R. Floreanini, *Physical Review A* **70**, 012112 (2004).

[59] S. Bhuvaneswari, R. Muthuganesan, and R. Radha, *Physica A* **604**, 127934 (2022).

[60] S. Elghaayda, A. Ali, M. Y. Abd-Rabbou, M. Mansour, and S. Al-Kuwari, *European Physical Journal C* **85**, 447 (2025).

[61] H.-W. Li, Y.-H. Fan, S.-T. Shen, X.-J. Yan, X.-Y. Li, W. Zhong, Y.-B. Sheng, L. Zhou, and M.-M. Du, *The European Physical Journal C* **84**, 1241 (2024), arXiv:arXiv:2411.19254 [quant-ph].

[62] J.-W. Hu and H.-W. Yu, *Physical Review D* **88**, 104003 (2013).

[63] V. Gorini, A. Kossakowski, and E. Sudarshan, *Journal of Mathematical Physics* **17**, 821 (1976).

[64] G. Lindblad, *Communications in Mathematical Physics* **48**, 119 (1976).

[65] M. A. Nielsen and I. L. Chuang, *Quantum Computation and Quantum Information* (Cambridge University Press, Cambridge, UK, 2010).

[66] M. Hu and H. Fan, *Science China: Physics, Mechanics & Astronomy* **63**, 230322 (2020).

[67] M. Hu and W. Zhou, *Laser Physics Letters* **16**, 045201 (2019).

[68] C. Macchiavello and G. M. Palma, *Physical Review A* **65**, 050301 (2002).

[69] E. Jaloum and M. Amazioug, *Physica Scripta* **100**, 055120 (2025).

[70] E. Jaloum, M. Amazioug, and S. Haddadi, *Scientific Reports* **15**, 1 (2025).

[71] S. A. Hill and W. K. Wootters, *Physical Review Letters* **78**, 5022 (1997).

[72] W. K. Wootters, *Physical Review Letters* **80**, 2245 (1998).

[73] S. A. Hill and W. K. Wootters, *Physical Review Letters* **78**, 5022 (1997).

[74] G. Adesso, A. Serafini, and F. Illuminati, *Physical Review A* **70**, 022318 (2004).

[75] G. Vidal and R. F. Werner, *Physical Review A* **65**, 032314 (2002).

[76] M. B. Plenio, *Physical Review Letters* **95**, 090503 (2005).

[77] F. M. Paula, T. R. Oliveira, and M. S. Sarandy, *Physical Review A* **87**, 064101 (2013).

[78] T. Nakano, M. Piani, and G. Adesso, *Physical Review A* **88**, 012117 (2013).

[79] F. Ciccarello, T. Tufarelli, and V. Giovannetti, *New Journal of Physics* **16**, 013038 (2014).

[80] E. Jaloum and M. Amazioug, *Nuclear Physics B* **117255** (2025).

[81] M. Amazioug and M. Daoud, *Physics Letters A* **493**, 129245 (2024).

[82] T. Baumgratz, M. Cramer, and M. B. Plenio, *Physical Review Letters* **113**, 140401 (2014).

- [83] M. D. Shaw, J. F. Schneiderman, J. Bueno, B. S. Palmer, P. Delsing, and P. M. Echternach, *Physical Review B* **79**, 014516 (2009).
- [84] L. Tian, L. Qin, and H. Zhang, *Chinese Physics Letters* **28**, 050308 (2011).
- [85] E. Albayrak, *International Journal of Modern Physics B* **27**, 1350055 (2013).
- [86] H. M. Soufy and C. Benjamin, *Physical Review A* **112**, 052215 (2025).
- [87] A. H. B. Pili, R. Khordad, H. R. R. Sedehi, and M. Sharifzadeh, *Physica B: Condensed Matter* **678**, 415748 (2024).